Expert decision support system for aeroacoustic source type identification using clustering

A. Goudarzi, C. Spehr and S. Herbold

Expert decision support system for aeroacoustic source type identification using clustering

A. Goudarzi,[1,a)] C. Spehr,[1,b)] and S. Herbold[2,c)]

[1]*German Aerospace Center (DLR), Germany*

[2]*Institute of Computer Science, University of Göttingen, Germany*

ABSTRACT:

This paper presents an Expert Decision Support System for the identification of time-invariant, aeroacoustic source types. The system comprises two steps: first, acoustic properties are calculated based on spectral and spatial information. Second, clustering is performed based on these properties. The clustering aims at helping and guiding an expert for quick identification of different source types, providing an understanding of how sources differ. This supports the expert in determining similar or atypical behavior. A variety of features are proposed for capturing the characteristics of the sources. These features represent aeroacoustic properties that can be interpreted by both the machine and by experts. The features are independent of the absolute Mach number, which enables the proposed method to cluster data measured at different flow configurations. The method is evaluated on deconvolved beamforming data from two scaled airframe half-model measurements. For this exemplary data, the proposed support system method results in clusters that mostly correspond to the source types identified by the authors. The clustering also provides the mean feature values and the cluster hierarchy for each cluster, and for each cluster member, a clustering confidence. This additional information makes the results transparent and allows the expert to understand the clustering choices.
© 2022 Acoustical Society of America. https://doi.org/10.1121/10.0009322

I. INTRODUCTION

Multiple noise-generating phenomena and mechanisms exist in aeroacoustics (Howe, 2007; Müller, 1979). To identify these phenomena in processed experimental data, expert domain knowledge and a detailed analysis of measurements are necessary. For the localization and estimation of the sound power of complex source geometries, such as planes, cars, or trains, beamforming is a reliable method (Merino-Martínez *et al.*, 2019). Beamforming results in high-dimensional maps of the Power Spectral Density (PSD) that are difficult and time-consuming to analyze manually. Therefore, the resulting beamforming maps are usually integrated over space and frequency areas to obtain low-dimensional data such as spectra (Merino-Martinez *et al.*, 2019) or Overall Sound Pressure Levels (OASPL), which human experts then analyze and interpret. For the identification of the source types or source mechanisms, experts often rely upon the spatial localization and meta-information, e.g., that sources are located at a trailing edge and, thus, are identified as trailing edge noise. For real-world vehicles or vehicle models, this information can be missing or misleading, since the geometries of interest are highly complex and result in a superposition of sound generating mechanisms. Therefore, identifying aeroacoustic source types is a complex, time-consuming task that requires experts to compare the analyzed data to simplified, generic, and controlled reference measurements. However, these reference measurements often do not reflect the behavior of real-world geometries due to mismatched Reynolds numbers, installation effects, and object modifications (e.g., tripping and empty nacelles in airframe models).

The goal of this paper is to overcome this obstacle by introducing a system that supports experts in the process of source identification by means of automated data processing and machine learning. There are two major categories for analyzing and structuring data: supervised learning and unsupervised learning. Supervised learning models an unknown function for known input data and a desired outcome. The desired outcome must be known, i.e., the data must be labeled with a ground truth (Bianco *et al.*, 2019; Mello and Ponti, 2018). However, the aeroacoustics of airframe noise and complex aircraft models is a field where it is not feasible at the moment to obtain a ground truth due to the complexity of sound generating mechanisms, such as turbulence-induced noise at high Reynolds numbers. For seemingly simple mechanisms like the shear layer induced noise of a jet, there exists no scientific consensus on the exact mechanism that is responsible for the observed far-field sound (Karabasov, 2010). Additionally, there is not yet enough data of complex, real-world aircraft models to employ supervised machine learning, since the wind tunnel measurements are costly and both model geometries and results are often confidential. Therefore, supervised learning is currently not a suitable approach for the presented task.

Instead, unsupervised learning will be used in this paper to predict similar source types or source mechanisms, which

a)Electronic mail: armin.goudarzi@dlr.de, ORCID: 0000-0002-2437-028X.
b)ORCID: 0000-0002-2744-3675.
c)ORCID: 0000-0001-9765-2803.

is called clustering. While these clusters cannot replace the manual analysis of the expert, they are supposed to help with identifying similar sound source types, interpreting their acoustic properties, and detecting typical and anomalous behavior. Such a method is referred to as an Expert Decision Support System (EDSS). Bioacoustics in coral reefs (Ozanich *et al.*, 2021) and the structural analysis of wind turbine bearings *via* their emitted sound (Ben Ali *et al.*, 2018) are examples for unsupervised learning, as the task of labeling requires either knowledge that is unavailable or too much time and resources (e.g., the turbines would have to be dissembled to obtain a ground truth). The sounds can be processed and presented to the clustering algorithm in many forms. However, since unsupervised learning not only models the function but also estimates an outcome, it is important that the variance within the data representation makes the desired clustering choice likely; e.g., to successfully cluster sounds of different animals, the data variance between the animals must be greater than the variance due to changes between the locations the sounds were recorded at. Otherwise, the clustering will result in clusters of different recording locations instead of different animals. This is achieved through data preprocessing, which includes the reduction of the data's dimensionality (e.g., the OASPL of a sound instead of time-domain data), and the reduction of complexity (e.g., using the PSD instead of the time-data). This preprocessing step and careful selection and definition of calculated properties with the goal to obtain a representation of the underlying data suitable for the clustering is called "feature engineering."

The paper is structured as follows. We use CLEAN-SC (Sijtsma, 2007) beamforming maps (Merino-Martínez *et al.*, 2019) of the scaled air-frame models of a Dornier 728 (Do728) (Ahlefeldt, 2013) and an Airbus A320 (A320) (Ahlefeldt, 2017) as example data, featuring multiple aeroacoustic source types. We employ the Source Identification based on spatial Normal Distributions (SIND) (Goudarzi *et al.*, 2021) approach to identify individual sources and obtain their spectra from the beamforming maps. We explain typical aeroacoustic properties and derive corresponding features, discuss their usefulness, and propose mathematical definitions. We then cluster the sources in the obtained feature space using HDBSCAN (Campello *et al.*, 2013). We present a manual identification of the airframe source types with exemplary spectra and our decision choices to the reader, which allows us to compare the resulting clusters to our source categories. We then evaluate which clusters are meaningful and correspond to our source categories, derive a corresponding confusion matrix, and calculate a clustering accuracy based on them.

The method reported in this paper was originally presented at the AIAA Aviation 2020 conference (Goudarzi *et al.*, 2020) as work-in-progress. This paper presents more data (five different Reynolds numbers for the Do728, and four for the A320 versus one for both models in the conference paper). It presents additional features, and some modified feature calculations, an in-depth analysis of the

TABLE I. Reynolds configurations of the Do728 dataset.

configuration	D1	D2	D3	D4	D5
$\langle \text{Re} \rangle_M [1 \times 10^6]$	1.4	1.8	2.5	3.8	10.6
$T[K]$	290	250	200	150	100
$p_0[1 \times 10^5 Pa]$	1.0	1.0	1.0	1.0	1.0

proposed features, and a statistical analysis and discussion of the clustering results.

II. DATASETS

The data used in the present paper consist of beamforming measurements of two closed-section wind tunnel models: one is of a Do728 (Ahlefeldt, 2013) and one is of an A320 (Ahlefeldt, 2017). Both models were observed at multiple Reynolds numbers $\langle \text{Re} \rangle_M$, angles of attack α, and Mach numbers M. For the Do728 model, the Mach-averaged Reynolds numbers $\langle \text{Re} \rangle_M$, the ambient pressures p_0 and cryogenic temperatures T are shown in Table I based on the mean aerodynamic cord length $D_0 = 0.353$m. With the dynamic viscosity $\mu(T)$ and density $\varrho(p_0, T)$ of the medium, the Reynolds number is

$$\text{Re} = \frac{\varrho(p_0, T)M(T, u)D_0}{\mu(T)}. \tag{1}$$

Values of $\alpha_a = [1°, 3°, 5°, 6°, 7°, 8°, 9°, 10°]$ were chosen for angle of attack for every Reynolds number configuration and $M_j = [0.125, 0.150, 0.175, 0.200, 0.225, 0.250]$ as Mach number for every angle of attack. In total, the Do728 dataset contains $5\langle \text{Re} \rangle_M \times 8\alpha \times 6M = 240$ different flow configurations. The array consisted of 144 microphones at an oval aperture of 1.756 m × 1.3 m and a data sample frequency of $f_S = 120$ kHz was used.

The A320 model was observed at $\alpha_a = [3°, 7°, 7.15°, 9°]$ for every Reynolds number configuration, and $M_j = [0.175, 0.200, 0.225]$ for every angle of attack. The Mach averaged Reynolds numbers, the ambient pressures p_0 and cryogenic temperatures T are shown in Table II based on $D_0 = 0.353$ m. In total, the A320 dataset contains 48 different flow configurations. The array consisted of 96 microphones at an aperture of 1.06 m × 0.5704 m and the data were recorded at $f_S = 150$ kHz. For both datasets the Cross-Spectral density Matrices (CSM) were calculated using Welch's method with a block size of 1024 samples and 50% overlap which resulted in around 7000 block averages for the Do728 and 9000 averages for the A320. The beamforming was performed using conventional beamforming

TABLE II. Reynolds configurations of the A320 dataset.

configuration	A1	A2	A3	A4
$\langle \text{Re} \rangle_M [1 \times 10^6]$	1.4	5.1	5.1	19.9
$T[K]$	310	311	125	120
$p_0[1 \times 10^5 Pa]$	1.10	3.99	1.15	4.19

1260   J. Acoust. Soc. Am. **151** (2), February 2022

Goudarzi *et al.*

(Merino-Martínez *et al.*, 2019) and CLEAN-SC deconvolution (Sijtsma, 2007) on a regular grid with a focus point resolution of $\Delta x_1 = \Delta x_2 = 5 \times 10^{-3}$ m. The focus plane for both models is around $\Delta x_3 \approx 1$ m away from the array and covers around 2m^2, which results in a total of 8×10^5 focus points per beamforming map.

III. METHODOLOGY

This section presents the methodology of the EDSS. First, the procedure is presented and compared to a manual source analysis. Second, the definition of an aeroacoustic source in this context is provided. Third, aeroacoustic properties are discussed and corresponding features are derived. Fourth, the clustering process based on the features is described. We will use italic indices to indicate the dimensionality of the variables. For averaging a variable v over its i-th dimension, we use $\langle v_i \rangle_i$,

$$\langle v_i \rangle_i = \frac{\sum_{i}^{I} v_i}{I}, \tag{2}$$

and for the corresponding standard deviation $\sigma_i(v_i)$,

$$\sigma_i(v_i) = \sqrt{\frac{\sum_{i}^{I} (v_i - \langle v_i \rangle_i)^2}{I}}. \tag{3}$$

A. Procedure

Figure 1 compares the proposed EDSS process to a standard manual source analysis process for beamforming maps PSD $(\vec{x}, f_i, M_j, \alpha_a, \text{Re}_e)$, which typically includes spatial variables $\vec{x}$, multiple frequencies or frequency intervals f_i, angles of attack α_a, Mach numbers M_j, and Reynolds numbers Re_e. In the manual process, multiple regions of interest (ROI) $R_r(\vec{x})$ are defined and spatially integrated to derive acoustic spectra PSD $(R_r, f_i, M_j, \alpha_a, \text{Re}_e)$. This first step is already a challenging task since the ROIs must only contain the individual sources to obtain individual source spectra, which can be only verified using the resulting spectra. This often requires several iterations, as described in the following. After definition, the ROI spectra are analyzed, which often requires expert knowledge and intuition. Based on the analysis the ROI are then redefined (e.g., if two separate sources are detected within a ROI). Based on the spectra at different Mach numbers, expert knowledge, intuition, and meta-information (e.g.,the source is located at a trailing edge and thus, must be trailing edge noise) aeroacoustic properties are derived, and the source type is then identified or vice versa. The main challenge for this process is the high dimensionality of the properties $P_k(R_r, f_i, M_j, \alpha_a, \text{Re}_e)$ and the requirement for an iterative approach.

In comparison, the EDSS aims at automating most of these tasks. First, the ROI definition $R(\vec{x})$ and spectra generation were shown to have the capacity to be automated using
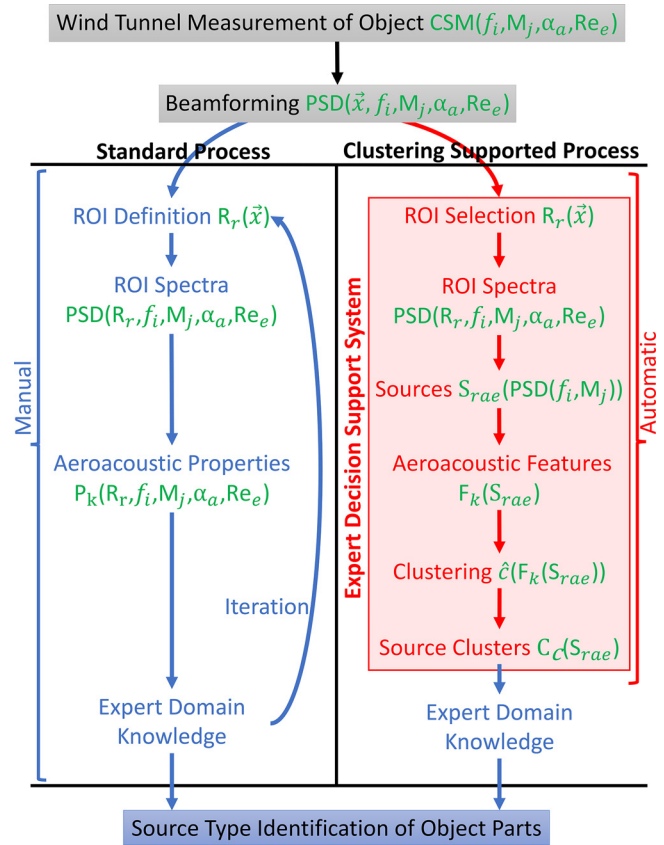

FIG. 1. (Color online) Comparison of the evaluation process of wind tunnel beamforming measurements. Left: a standard process using manual analysis. Right: the proposed Expert Decision Support System. Manual processing steps are displayed in blue while automatic steps are displayed in red. The resulting variables of each step are displayed in green. The indices indicate the dimensionality of these variables.

the SIND method (Goudarzi *et al.*, 2021). The EDSS then defines a source S_{rae} for each ROI R_r, at each angle of attack α_a, and at each Reynolds number Re_e. This results in multiple sources $S_{rae}[\text{PSD}(f_i, M_j)]$, for which aeroacoustic features $F_k(S_{rae})$ are then calculated. Finally, the sources are clustered based on the k-dimensional feature space with the process $\widehat{c}(F_k)$ which results in a cluster prediction for each source $C_c(S_{rae})$. This provides c-dimensional prediction information (each source is assigned to a cluster). Also, additional information about the similarity of source groups based on their cluster-averaged features is provided. The source types can then be identified manually based on the expert's knowledge and the low-dimensional information provided by the EDSS.

B. Source definition

An aeroacoustic source emerges either from the interaction of an obstacle placed in a flow, e.g., a cylinder (Zdravkovich, 1997) or from the flow itself, e.g., jet noise (Lighthill and Newman, 1952). When we observe a source at a specific flow speed or angle of attack, the observed source is often a realization of one or more underlying physical mechanisms. These mechanisms often result in

J. Acoust. Soc. Am. **151** (2), February 2022

Goudarzi *et al.* 1261

observations that change continuously over variations of flow parameters such as the Mach or Reynolds number. To distinguish between different source mechanisms, we have to identify the underlying parameters for which the source mechanism is self-similar. The observable variables depend on the measurement matrix in controlled wind tunnel experiments. They can be the angle of attack α, wind speed u, Mach number M, temperature T, and ambient pressure p_0. The variation in pressure and temperature changes the Reynolds number, the variation of the wind speed, and the temperature changes the Mach number. Wind tunnel facilities often use scaled models, increased total pressures, and a lowered temperature to achieve high, real-world Reynolds numbers (Ahlefeldt, 2013). Thus, the result of beamforming in wind tunnels is a high-dimensional sound power map $\mathrm{PSD}(\vec{x}, f, M(T, u), \alpha, \mathrm{Re}(T, u, p_0))$.

A basic assumption in aeroacoustic source modeling is that small changes in subsonic Mach numbers do not alter the source mechanism (Howe, 2007). Also, a source may exist in extended spatial areas or frequency intervals, for instance, the sound generated from vertices in Kármán's vortex street (Prandtl and Tietjens, 1957; Zdravkovich, 1997). Sources may have a frequency-dependent spatial location and shift their peak frequencies with changing Mach number. One example is jet noise where the location of dominant sound generation shifts downstream and the peak frequency decreases with increasing Mach number, while the PSD level increases (Lighthill and Newman, 1952). However, a normalization of the PSD or frequency using the Mach number reveals that the spectrum shape, Mach-normalized peak frequencies, and Mach-normalized PSDs collapse (Quinlan and Krane, 1996). This is referred to as self-similarity. The underlying physical sound-generating mechanism has not changed, we only observe a different realization of the source mechanism. However, source mechanisms can change completely for large variations of their Reynolds numbers. One example of this is the radiated acoustics from a flow around a cylinder (Zdravkovich, 1997), where the flow properties may change due to, for instance, the transition from a laminar to a turbulent flow. Thus, only small subsonic Mach number changes are considered. All other variations such as the angle of attack α or changes in geometry may alter the dominant source mechanism abruptly (e.g., slat tones and flow separation in airframe noise may appear). We treat these variations as potentially different source mechanisms.

Since we are interested in clustering the sources according to their underlying physical mechanisms rather than clustering them by their dominance, we need to analyze the scaling behavior over Mach number and the similarity laws (Howe, 2007) rather than absolute levels at specific Mach numbers. Therefore, we define the properties of a source as follows. First, a source is connected to a spatial region $R(\vec{x})$. Second, when a source is observed at a different Mach number, it is still the same source. Third, a source may be observed for small variations of the Reynolds number due to the change of the Mach number. A large variation of the

Reynolds number to changes in temperature or pressure results in a different source. Fourth, any change of the angle of attack results in a different source. Based on this definition a sound source's PSD, obtained from the spatially integrated ROI, possesses the free variables $\mathrm{PSD}(f, M)$ at a fixed $\langle\mathrm{Re}\rangle_M$ and α. For example, a ROI $R(\vec{x})$ that was identified by SIND within the Do728 beamforming maps is treated as unique sources for each angle of attack and Mach averaged Reynolds number (which results in $8\alpha \times 5\langle\mathrm{Re}\rangle_M = 40$ individual sources for any identified spatial ROI), each represented by six spectra at different Mach numbers $M = [0.125, \ldots, 0.250]$. Since we assign multiple spectra of measurements at different Mach numbers to one source, we can derive its acoustic properties not only from the individual spectra but from the changes over Mach number or as an average property of the spectra. This has the advantage, that the Mach-normalized features of different datasets are comparable despite their measurement at different Mach numbers. Additionally, the averaging reduces the uncertainty of the feature estimation.

C. Feature engineering

We require a set of features that describe the aeroacoustic properties of a source for clustering. For optimal clustering results and interpretability of the results we require a feature-set that meets the following conditions:

- All features together must unambiguously describe a source or its mechanism.
- A feature must describe a basic property of a source and must provide additional information.
- The calculation of a feature must be automatable and robust.
- A feature must be represented by a single numerical value.
- A feature must correspond to a physical property.

In real-world applications, it is typically not possible to fulfill these requirements completely. Additionally, it can only be analyzed how well the introduced features meet these requirements in the context of the observed sources. In the following section, we identify aeroacoustic properties and break them down to numerical features in the subsequent sections. A complete list of the features is given in Table III. We will present the resulting feature values in the results section and discuss how well the proposed features meet the conditions in Sec. VI.

1. Broadband self-similarity

An important property of any aeroacoustic source is the self-similarity or scaling behavior over increasing Mach number. An acoustic spectrum that exhibits self-similarity over the Strouhal number indicates a physical source mechanism that is connected to the flow such as turbulence-induced noise (Lighthill and Newman, 1952). With the speed of sound a, the Strouhal number is defined as

1262   J. Acoust. Soc. Am. **151** (2), February 2022

Goudarzi *et al.*

TABLE III. Table of all aeroacoustic properties, their corresponding features, their variables, equations, if they are used logarithmically with $\log(|v|+1)$, and their (log) value range.

property	feature	var.	Eq.	log	range
Self-similarity	scal. over St number	scal(St)	(9)	No	$[0,1]$
	scal. over He number	scal(He)	(9)	No	$[0,1]$
	freq. norm. exp.	$m^\star$	(11)	No	$[0,\infty[$
Power scaling	M scal(St)	n_{St}	(15)	No	$[0,\infty[$
	M scal(He)	n_{He}	(15)	No	$[0,\infty[$
Tonality	Number of tones	$\widehat{P}_n$	(17)	Yes	$[0,\infty[$
	Tone St shape	k_{St}	(18)	Yes	$[0,\infty[$
	Tone St scale	θ_{St}	(18)	Yes	$[0,\infty[$
	Tone St loc	l_{St}	(18)	Yes	$[0,\infty[$
	Tone width shape	k_w	(18)	Yes	$[0,\infty[$
	Tone width scale	θ_w	(18)	Yes	$[0,\infty[$
	Tone width loc	l_w	(18)	Yes	$[0,\infty[$
	Tone prom shape	k_p	(18)	Yes	$[0,\infty[$
	Tone prom scale	θ_p	(18)	Yes	$[0,\infty[$
	Tone prom loc	l_p	(18)	No	$[0,\infty[$
	scal. over St number	$scal_p(St)$	(21)	No	$[0,1]$
	scal. over He number	$scal_p(He)$	(21)	No	$[0,1]$
	Tone intensity	$prop_p$	(22)	No	$[0,1]$
Source loc.	Source movement	Δl	(23)	No	$[0,\infty[$
Spatial dist.	Source compactness	A	(24)	No	$[0,\infty[$
	Source shape	R_σ	(25)	Yes	$[0,\infty[$
Spectrum shape	Regression slope	$\widehat{s}$	(26)	Yes	$[0,\infty[$
	Regression r^2-value	r^2	(28)	no	$[0,1]$
	Avg. St number	$\overline{St}$	(30)	yes	$[0,\infty[$
	std. St number	St_σ	(31)	yes	$[0,\infty[$
	PSD_{max} St number	St_{Lmax}	(32)	yes	$[0,\infty[$

$$St = \frac{fD_0}{Ma}. \tag{4}$$

Spectra collapsing over the use of Helmholtz number,

$$He = \frac{fD_0}{a}, \tag{5}$$

indicate a mechanism connected to acoustic resonances (Müller, 1979) or radiation effects (Michalke, 1977) due to spatial coherence of a non-compact source. If a source is self-similar over one of these frequency types (we refer to the absolute frequency, the Helmholtz number, and the Strouhal number as frequency types), there is a linear dependency between the PSD levels over frequency at different Mach numbers. Thus, we calculate the Pearson correlation coefficients $\rho_{jj'}$ between all spectra at different Mach numbers M_j and $M_{j'}$,

$$\rho_{jj'} = \sum_i^I \left[(PSD(M_j, f_i)) - \langle PSD(M_j, f_i) \rangle_i \right. $$
$$\times (PSD(M_{j'}, f_i)) - \langle PSD(M_{j'}, f_i) \rangle_i) \right] $$
$$\times \left[\sigma_i(PSD(M_j, f_i))\sigma_i(PSD(M_{j'}, f_i)) \right]^{-1}. \tag{6}$$

Note that for the calculation of Eq. (6) using the Strouhal or Helmholtz number, the spectra have to be interpolated on

the same Strouhal or Helmholtz number vectors for different Mach numbers. For the results presented in this paper, we use linear interpolation on a logarithmic Strouhal and Helmholtz number vector with 12 bins per octave. Since the correlation matrix is symmetric and the diagonal entries are unity, we determine the Mach average $\overline{corr}$ and standard deviation $corr_\sigma$ of the correlation coefficients using the upper triangular matrix $j > j'$ with $J = |M_j|$,

$$\overline{corr} = \frac{2}{J(J-2)} \sum_{j>j'} \rho_{jj'}, \tag{7}$$

$$corr_\sigma = \sqrt{\frac{2}{J(J-2)} \sum_{j>j'} (\rho_{jj'} - \overline{corr})^2}. \tag{8}$$

Most aeroacoustic spectra decay in SPL over frequency and if this decay is stronger than local structures or peaks in the spectra, this can result in strong correlations for frequency types over which the spectra are not self-similar. However, the correlation matrix $\rho_{jj'}$ then often exhibit great variance. Thus, a mean correlation $\overline{corr}$ is not an optimal definition for the self-similarity. It can be improved by taking its standard deviation $corr_\sigma$ and the mean p-value $\bar{p}$ into account. The p-values are averaged as shown in Eq. (7) and represent the reliability of the correlation estimation. Due to the beamforming process in combination with CLEAN-SC, the discrete spectra often contain missing values. If we drop the corresponding frequencies f where $PSD(M,f) = -\infty \, dBHz^{-1}$ before the calculation, the standard deviation, and the p-value will increase drastically due to the decreasing sample size when the spectra are not self-similar. Using these properties, we introduce the final broadband self-similarity (scal),

$$scal = (\overline{corr} - corr_\sigma)(1 - \bar{p}), \tag{9}$$

which can be calculated over all frequency types separately. This definition strongly penalizes a high p-value and a large variance in the correlations.

2. Frequency normalization exponent

As stated in Sec. III C 2 a spectrum scales either over the Strouhal or the Helmholtz number. However, we observe in the presented data that spectra that are supposed to scale over the Strouhal number are often not perfectly aligned as depicted in Fig. 1(a). In this rare case of multiple cryogenic measurement conditions, both datasets allow us to observe spectra at constant absolute Reynolds number over increasing Mach number (at decreasing temperatures and increasing pressure). Using spectra spectra at different Mach numbers from different Reynolds configurations so that the absolute Reynolds number is kept constant, the spectra are perfectly aligned (not depicted here). Thus, the increase in Reynolds number over Mach number at constant pressure and temperature may cause sources to decrease or increase the Strouhal numbers dependence on the Mach number.

J. Acoust. Soc. Am. **151** (2), February 2022

Goudarzi *et al.* 1263

Since cryogenic measurements are rare and expensive, we assume that many datasets are observed at constant pressure and temperature (i.e., different absolute Reynolds numbers) and are affected by this phenomenon. To overcome this problem, we define a modified normalized frequency $\widehat{f}$ that compensates for this altered Mach dependency by introducing the generalized frequency normalization exponent m. We then define the modified normalized frequency as

$$\widehat{f} = \frac{fD_0}{M^m a}. \tag{10}$$

Note that this normalized frequency is a generalization of the Helmholtz number (for $m = 0$) and the Strouhal number (for $m = 1$). For convenience, we will speak of a modified Strouhal number if $m \geq 0.5$. To obtain the generalized frequency normalization exponent, we optimize the collapse of the spectra by maximizing its broadband self-similarity (see Sec. III C 1). Figure 2 shows the comparison of the normal Strouhal number [Fig. 2(a)] and the modified Strouhal number with $m = 0.72$ [Fig. 2(b)]. Figure 2(c) shows the mean spectra correlation $\overline{\mathrm{corr}}$ (black line), and its standard deviation corr_σ (gray area) over the modification exponent m. The blue line is the mean p-value $\bar{p}$, indicating the reliability of the correlation estimation. The optimal value $m^\star$ (shown with the red x) is achieved at the global maximum of the self-similarity, see Eq. (9),

$$m^\star = \underset{m \in [0,\infty]}{\mathrm{argmax}}(\mathrm{scal}(m)). \tag{11}$$

In the example of these slat tones, the increase in Reynolds number results in a weaker Mach dependency of the normalized frequency than a regular Strouhal number.

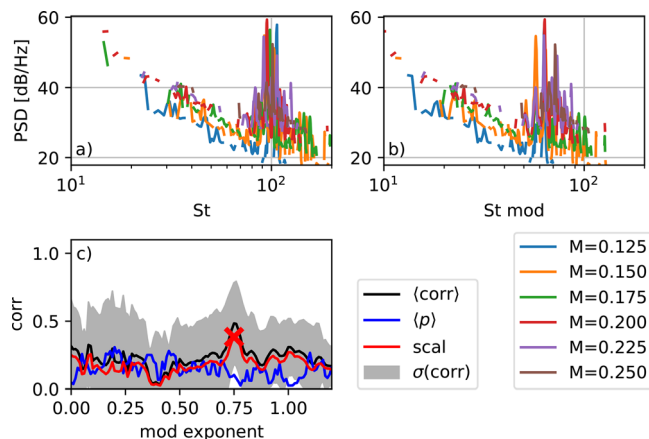The following acoustic properties are derived from spectra at different Mach numbers, which can be displayed over the Strouhal number, the Helmholtz number, or the introduced modified normalized frequency. Since aeroacoustic experts are used to analyzing spectra displayed over Strouhal and Helmholtz number, we calculate features from spectra displayed over both Helmholtz and modified Strouhal number separately. If a spectrum is dominated by a Helmholtz number scaling mechanism, the frequency modification exponent will result in values $m \approx 0$. To present spectra over both Helmholtz and (modified) Strouhal number, we have to find a local maximum of the self-similarity function around $m_{\mathrm{St}} \approx 1$ to account for spectra that include minor, Strouhal number scaling mechanisms. To do so, we run a standard peak detection over the self-similarity function $\mathrm{scal}(m)$ to find a local maximum $\tilde{m} \geq 0.5$ with a peak prominence $\widehat{P}_{\mathrm{p}} \geq 0.1$. If none is found and $m^\star < 0.5$, we simply set $m_{\mathrm{St}} = 1$ to obtain a Strouhal number,

$$\tilde{m} = \underset{\substack{m \in [0.5, \infty] \\ \max(\widehat{P}_{\mathrm{p}}) \geq 0.1}}{\mathrm{peak}}(\mathrm{scal}(m)), \tag{12}$$

$$m_{\mathrm{St}} = \begin{cases} m^\star & \text{if } m^\star > 0.5, \\ \tilde{m} & \text{if } m^\star \leq 0.5, \\ 1 & \text{else.} \end{cases} \tag{13}$$

3. Sound power scaling

The power of aeroacoustic noise generally increases with increasing Mach number. A prominent example is jet noise for which Lighthill derived the M^8 scaling law (Lighthill and Newman, 1952). Thus, when doubling the Mach number, the PSD will increase by $10\log_{10}(2^8) = 24\,\mathrm{dB}$. The power scaled PSDs ($\widehat{\mathrm{PSD}}$), with the power scaling exponent n, are given by

$$\widehat{\mathrm{PSD}}(f_i, M_j) = \mathrm{PSD}(f_i, M_j) - n10\log_{10}(M_j). \tag{14}$$

Conventionally, a regression on the OASPL (which is the sound power integrated over frequency) or peak levels of Eq. (14) is used to determine n. This does not always work for spectra from beamforming maps, since the microphone array aperture in combination with deconvolution acts like a high-pass filter at an absolute frequency. This is problematic when scaling over the Strouhal number (and Helmholtz number at different temperatures and pressures). It effectively creates a Mach dependent low-cut filter, which in combination with a typical SPL decrease over frequency for aeroacoustic sources, results in a wrong OASPL and thus scaling exponent. Instead, we minimize the mean distance between all power scaled spectra $\widehat{\mathrm{PSD}}(f_i, M_j)$ over frequency bin-wise with a standard bounded minimization algorithm. To calculate a distance between multiple spectra at once we use the standard deviation σ of the spectra at every discrete frequency. Since parts of a spectrum with a high SPL are often considered more important for the scaling, we can weight the standard deviations at every frequency with the Mach averaged spectrum power

FIG. 2. (Color online) Do728, $\mathrm{Re} = 1.4 \times 10^6$, slat tones at $\alpha = 8°$. Comparison of source spectra at different Mach numbers over (a) normal Strouhal number and (b) modified Strouhal number, see Eq. (10), with $m = 0.74$; (c) shows the mean and standard deviation σ of the Pearson correlation coefficient of the source spectra at different Mach numbers over the variation of the modification exponent, the mean p-value, and the resulting self-similarity (scal), see Sec. III C 1. The modification exponent $m = 0.74$ achieves the optimal self-similarity, marked with an x.

1264   J. Acoust. Soc. Am. **151** (2), February 2022

Goudarzi *et al.*

$\langle \text{PSD}(f_i, M_j) \rangle_{M_j}^{\kappa}$. The hyperparameter κ of this weight determines by how much we want to prefer the scaling of high levels. Thus, we minimize

$$\min_{0 \le n < \infty} \sum_i \left[\sigma_j(\text{PSD}(f_i, M_j) - n10 \log_{10}(M_j)) \langle \text{PSD}(f_i, M_j) \rangle_j^{\kappa} \right],$$
(15)

with $n, \kappa \in \mathbb{R} \ge 0$. For the calculation of a reliable power scaling exponent at least spectra at three different Mach numbers should be used. A large variation in Mach number also increases the scaling's reliability. Figure 3 shows the resulting power scaling for a slat/slat track source and $\kappa = 10$ over modified Strouhal number and Helmholtz number. Note the different scaling behavior over Strouhal and Helmholtz number for the low and high-frequency part of the spectrum and that the OASPL scaling n_{OASPL} obtained by a linear regression neither matches the Helmholtz nor the Strouhal scaling exponent correctly, as described above. In Fig. 7, more examples of scaled PSDs with $\kappa = 10$, which was used for all results presented in this paper, are displayed.

4. Tonality

Accounting for the tonal behavior of the sources results in less straightforward feature descriptions since the tonal peaks vary from source to source and within a source for different Mach numbers but their properties must be captured by a finite amount of features, see Sec. III C. These properties are the peak width intervals $\widehat{P}_{\text{w}}$, peak prominences $\widehat{P}_{\text{p}}$, peak frequencies $\widehat{P}_{\text{f}}$, and the number of peaks $\widehat{P}_{\text{n}}$. First, we run a standard automated peak detection over the spectra, which results in a set of peak prominences $P_{\text{p}}(M_j)$, peak widths $P_{\text{w}}(M_j)$, and peak frequencies $P_{\text{f}}(M_j)$ for every Mach number M_j. Additionally, we define sets of frequency bins $P_{\tilde{\text{f}}}(M_j)$ that include all frequency bins, that lie within the peak width intervals $P_{\text{w}}(M_j)$,

$$P_{\tilde{\text{f}}}(M_j) = \{f_i | s.t. f_i \text{ belongs to a peak for } M_j\}.$$
(16)

The number of peaks $\widehat{P}_{\text{n}}$ is defined as the Mach averaged number of elements in the sets,

$$\widehat{P}_{\text{n}} = \langle |P_p(M_j)| \rangle_j.$$
(17)

As stated in Sec. III C, we have to break down the properties of the peaks to single value features. We do so by describing the distribution of the peaks' properties instead of using the individual peaks' properties directly. Naturally, peaks with lower prominence appear more often than peaks with very high prominence in P_{p}. This assumption is also used for the peak width in P_{w}. This behavior can be modeled using a gamma distribution (Abramowitz, 1974). With the gamma function $\Gamma(k)$, the Probability Density Function (PDF) γ of the gamma distribution over a variable v with a shape k, scale θ and location l is

$$\gamma(v, k, \theta, l) = \frac{(v-l)^{k-1} \exp\left(-\frac{v-l}{\theta}\right)}{\theta^k \Gamma(k)} \quad \text{for} \quad v, k, \theta, l \ge 0.$$
(18)

For the peak frequency locations in P_{f}, we found that a lognormal distribution fits most of the sources best. The distributions of these properties have unknown shape (standard deviation), scale (distribution median), and location (distribution offset) parameters which can be approximated from any number of samples greater than one by fitting the gamma or lognormal distribution to the data with standard fitting methods. The shape, scale, and location for peak width, peak prominence, and peak frequency are used as comparable feature values, independent of the number of tones in the PSDs and the number of different Mach numbers. Figure 4 shows the peak detection and the corresponding distributions for all Mach numbers of a Do728 slat tone source. We set a lower threshold of 3 dB for the peak prominence to prevent the algorithm from detecting lots of irrelevant low-level peaks which dominate the distributions. We set the feature values to zero if only one or fewer tones are detected.

To determine how well the prominent peaks scale over Strouhal or Helmholtz number (scal$_{\text{p}}$) we average the ratio of how many peaks overlap at every detected peak frequency interval. Working with logarithmically spaced, discrete frequencies f_i, we introduce two sets. E_i are I sets, each
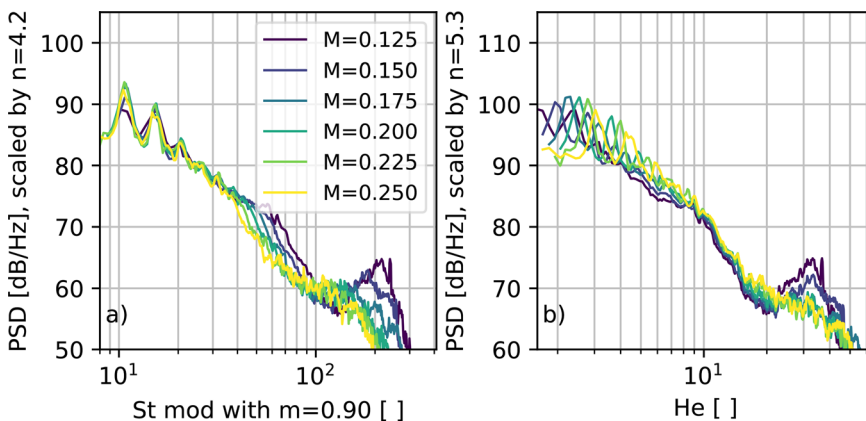

FIG. 3. (Color online) Do728 slat/slat track source at Re $= 1.4 \times 10^6, \alpha = 3°$. Comparison of the power scaling over modified Strouhal ($m = 0.9$) and Helmholtz number to collapse the PSDs with Eq. (14). The scaling exponents are $n_{\text{St}} = 4.2$, $n_{\text{He}} = 5.3$, $n_{\text{OASPL}} = 6.3$.
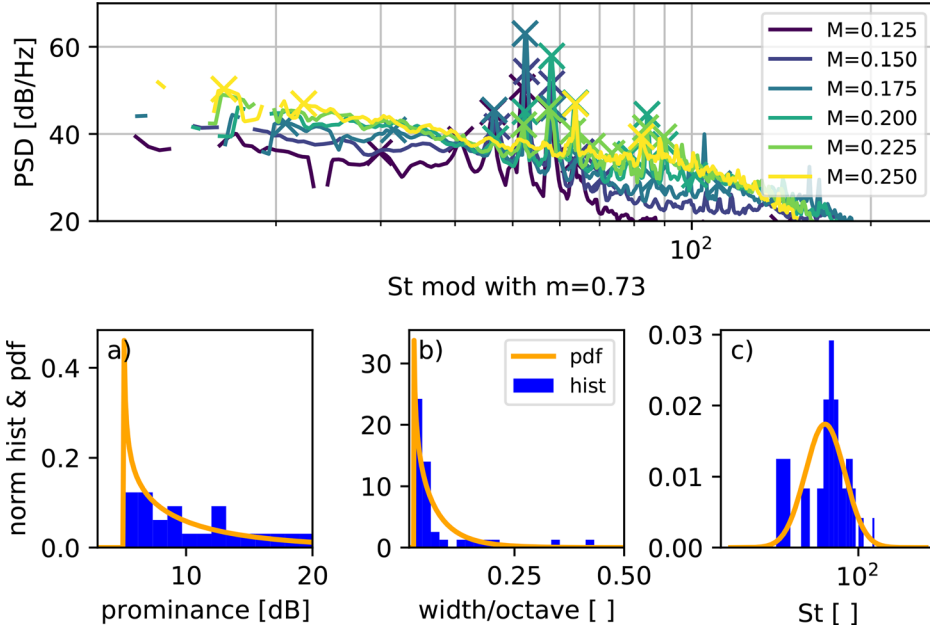
J. Acoust. Soc. Am. **151** (2), February 2022

Goudarzi et al.   1265

FIG. 4. (Color online) Do728, Re $= 1.4 \times 10^6$, slat tones at $\alpha = 8°$. Top, the spectra and the automatically detected peaks, depicted with an x. Bottom, a normalized histogram and the fitted PDF of the (a) peaks prominence, (b) peak width, and (c) peak Strouhal number.

containing up to J Mach numbers for which the frequency bin of the corresponding spectrum lies within a peak interval. $\hat{I}$ is a single set that contains the frequency indices i for which at least one spectrum features a peak,

$$E_i = \{M_j| \quad \text{so that} \quad f_i \in P_{\tilde{f}}(M_j)\}, \tag{19}$$

$$\hat{I} = \{i|\exists M_j \quad \text{so that} \quad f_i \in P_{\tilde{f}}(M_j)\}. \tag{20}$$

The resulting scaling of the tones is then the ratio of spectra that share a peak at the same frequency to the total number of spectra at different Mach numbers J, averaged over all frequency bins i for which at least one peak was detected,

$$\text{scal}_p = \frac{1}{|\hat{I}|} \sum_{i \in \hat{I}} \frac{|E_i| - 1}{J - 1}. \tag{21}$$

The minus ones ensure a soft feature value $0 \leq \text{scal}_p \leq 1$ for the modified Strouhal and Helmholtz number, since each E_i contains at least one element. Finally, we introduce the tonal intensity prop_p, defined as the Mach averaged ratio of tonal SPL to total SPL. It expresses how much percent of the energy in the spectra is caused by tones,

$$\text{prop}_p = \left\langle \frac{\sum_{f_i \in P_w(M_j)} \text{PSD}(f_i, M_j)}{\sum_i \text{PSD}(f_i, M_j)} \right\rangle_j. \tag{22}$$

5. Source location dependency on the Mach number

The spatial location of some aeroacoustic sources may change with the Mach number. An example of a moving source would be a flow detachment, at which the sound generating eddies move further downstream with increasing Mach number or jet noise, while cavity noise would remain

at the same location. Figure 5(a) shows the variation of source positions on the Do728 with increasing Mach number. For a numeric feature description, we calculate the positional change of the source with increasing Mach number and call it the source movement. We define the source movement Δl as the mean movement of the local source position $\vec{x}$, normalized by the change in Mach number, shown in Fig. 5(b). A limitation of this feature is that it assumes the monotonous movement of the source in one direction with the Mach number,

$$\Delta l = \left\langle \frac{|\vec{x}_j - \vec{x}_{j-1}|}{M_j - M_{j-1}} \right\rangle_j \quad \text{for } j \geq 2. \tag{23}$$

6. Spatial source distribution

Aeroacoustic sources can be spatially distributed, such as line or volume sources. We use the sources' spatial PDFs obtained with SIND to describe this behavior. SIND approximates the spatial source distributions with two-dimensional (2D) normal distributions, described by the standard deviations σ_{x_i}. We define the integrated, normalized PDF area A as a feature for the spatial compactness of the source,

$$A = \int_{x_1} \int_{x_2} \frac{\text{PDF}(x_1, x_2)}{||\text{PDF}(x_1, x_2)||_\infty} dx_2 dx_1$$
$$= 2\pi \sigma_{x_1} \sigma_{x_2}. \tag{24}$$

We define the ratio of the PDFs standard deviations σ_{x_i} as an indicator for line sources with

$$R_\sigma = \max\left(\frac{\sigma_{x_1}}{\sigma_{x_2}}, \frac{\sigma_{x_2}}{\sigma_{x_1}}\right) - 1. \tag{25}$$

Thus, $R_\sigma \approx 0$ indicates a point or sphere-like source while an increasing R_σ indicates a line source.
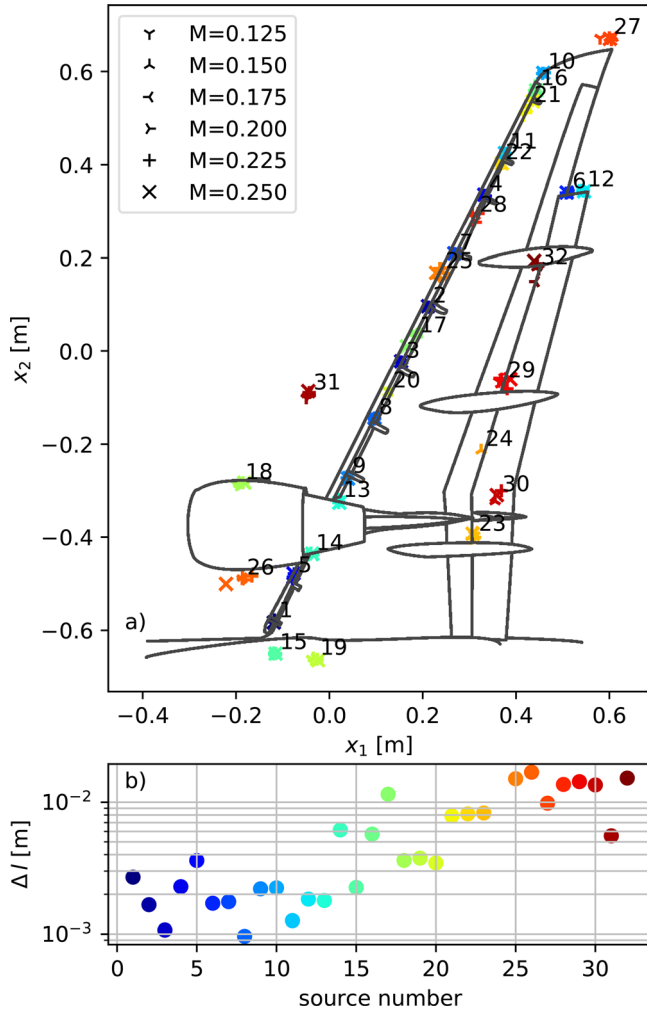
FIG. 5. (Color online) Do728 (a) shows the source positions at Re = 1.4 ×10⁶, $\alpha = 10°$ (if the source is present at this configuration) for the given Mach numbers. (b) Shows the mean movement of the sources calculated with Eq. (23).

7. Spectrum shape

To capture the general spectrum shape, we use a linear regression $L(f)$ for $\mathrm{PSD}(f)$, which consists of two values: the interception i_0 of the line at $f = 0\,\mathrm{Hz}$ and the slope $\hat{s}$,

$$L(f) = \hat{s}f + i_0. \tag{26}$$

The interception is an absolute value, varies with the Mach number, and is, therefore, discarded. The slope is the increase or decrease in the PSD level over the frequency. Additionally, we use the regression's r^2-value, which describes how well the linear regression explains the spectrum. A low r^2 value indicates that the linear regression is not capturing the movement in the spectrum well. Thus, it is an indication of the waviness of the spectra. With the error e of the regression model,

$$e_{ij} = \mathrm{PSD}(f_i, M_j) - L(f_i, M_j), \tag{27}$$

the Mach-averaged r^2 value is then calculated with

$$r^2 = \left\langle 1 - \frac{\sum\limits_i e_{ij}}{\sum\limits_i (\mathrm{PSD}_{ij} - \langle \mathrm{PSD}_{ij} \rangle_i)^2} \right\rangle_j. \tag{28}$$

Similar to the spatial source distribution, we define a source distribution over frequency. Since we work on sparse spectra which are not defined on all frequency bins, we use the mean $\bar{f}$ and standard deviation f_σ of the frequencies for which the source PSD is real valued to capture the source's radiation frequency interval. With the sets Q_j that contain the real valued frequency bins f_i for the spectra at Mach number M_j,

$$Q_j = \{f_i| \quad \text{such that} \quad \mathrm{PSD}(f_i, M_j) \in \mathbb{R}\}, \tag{29}$$

$$\bar{f} = \frac{1}{J} \sum_j \left(\frac{1}{|Q_j|} \sum_{f \in Q_j} f \right), \tag{30}$$

$$f_\sigma = \sqrt{\frac{1}{J} \sum_j \left(\frac{1}{|Q_j|} \sum_{f \in Q_j} (f - \bar{f})^2 \right)}. \tag{31}$$

Finally, we introduce the frequency $f_{L\max}$ for which the PSD level has a maximum,

$$f_{L\max} = \langle \mathrm{argmax}_i(\mathrm{PSD}(f_i, M_j)) \rangle_j. \tag{32}$$

D. Source clustering

We employ unsupervised clustering that groups the sources based on a distance metric in the introduced aeroacoustic feature space. We select Hierarchical Density-Based Spatial Clustering of Applications with Noise (HDBSCAN) (Campello et al., 2013; McInnes et al., 2017), which supports soft clustering without prior knowledge about the number of clusters, i.e., an expectation of the number of different source types. HDBSCAN also provides a clustering confidence. Since the distances between sources in a high dimensional feature space become alike (Aggarwal et al., 2001), the feature space must be reduced. The most prominent dimensionality reduction technique is Principal Component Analysis, which orthogonalizes the feature space and sorts the dimensions based on their explained variance. Then, dimensions with little statistical variance can be discarded. For the presented method, we use a Kernel Principal Component Analysis (KPCA) (Schölkopf et al., 1998) with a Radial Basis Function (RBF) as a kernel. The KPCA uses a nonlinear convolution kernel, which allows the PCA to embed the feature space in a nonlinear manifold. For dimensionality reduction, we retain $2\sigma \approx 95\%$ of the explained variance by discarding the KPCA dimensions with the least variance. Before using a PCA or KPCA, the feature space must be normalized to zero mean and unity variance. This normalization assumes that the features are normally distributed. However, most of the features F are

J. Acoust. Soc. Am. **151** (2), February 2022

Goudarzi et al. 1267

distributed exponentially and are transformed to a log-space prior to the KPCA with $\log_{10}(F+1)$, see Table III. Thus, the feature space is partially transformed into a log-space, then normalized, then orthogonalized and reduced to 95% explained variance using a KPCA, and then clustered using HDBSCAN.

HDBSCAN requires a minimum sample size which determines how many source members a cluster must have. Smaller clusters are discarded as noise. We can determine a reasonable sample size by examining the resulting cluster numbers. With an increasing sample size, the resulting number of clusters first drops massively and then decreases only slightly. Figure 6 demonstrates this for the Do728 dataset. We pick the sample size after which the total quantity of clusters $n_{clusters}$ only decreases slightly, in this case around $n_{samples} = 7$. This is sometimes referred to as the "elbow-method" or "knee-method" (Thorndike, 1953). It is noteworthy that picking a bad sample size may result in sub-clusters (splitting a cluster) or super-clusters (merging clusters), but the overall results remain comparable. Thus, it can be helpful to start with a large sample size to obtain few clusters which are manageable to analyze manually and then transition towards smaller sample sizes. We call the described methodology for this EDSS "Clustering sources based on their aeroacoustic features" (CRAFT).

IV. MANUAL SOURCE IDENTIFICATION

To visualize, analyze, and quantify the results of the EDSS, we first manually identify source types and label the sources in the Do728 and A320 datasets based on their spectra and their self-similarity. The labels for the manually identified source types are mainly chosen based on the sources' spatial location. We also compare the source spectra to each other to identify sub and super-categories. To make this process transparent to the reader, we present in Fig. 7 exemplary Do728 spectra for the most common categories. The sources in the left column are displayed over the modified Strouhal number and sources in the right column are displayed over the Helmholtz number. We note that the manual source type identification and label choices may be ambiguous, contain errors, and misinterpretations. Also, we emphasize that the source groups and corresponding labels cannot be held as ground truth, since they have not been obtained by independent researchers:
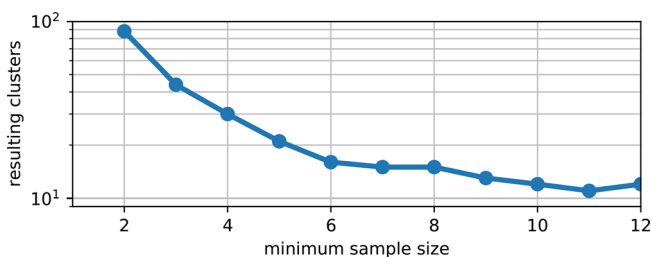

FIG. 6. (Color online) Do728, the figure shows the resulting numbers of clusters from HDBSCAN over the minimum sample size parameter.
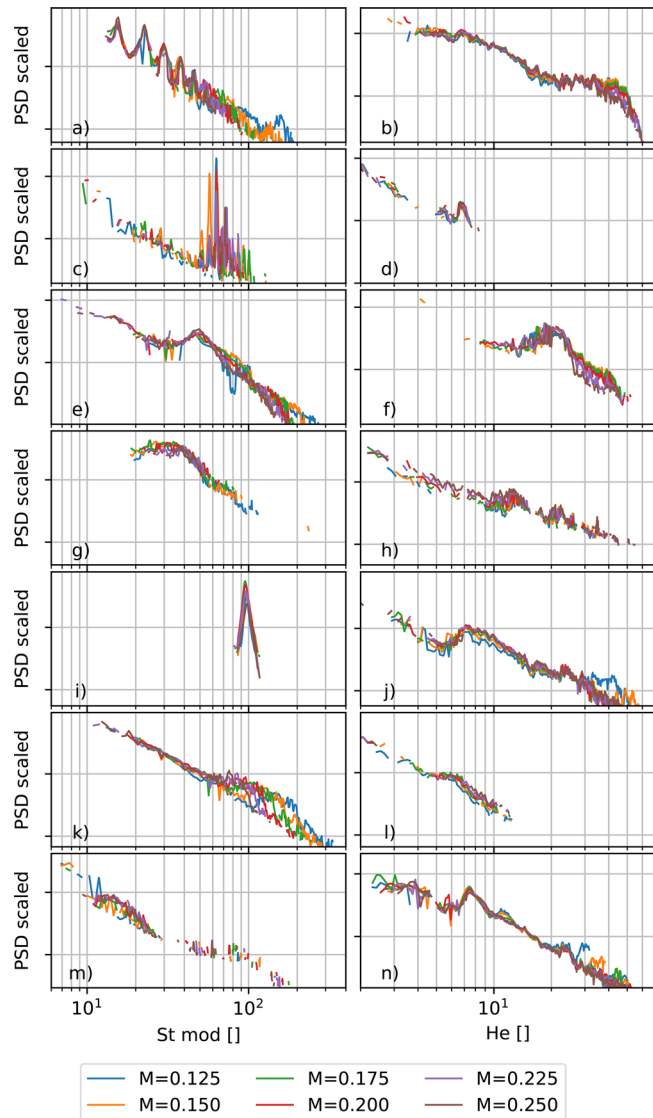
FIG. 7. (Color online) Do728, normalized spectra of the typical source types: (a) slat, (b) slat track, (c) slat tone, (d) flap tone, (e) trailing flap side edge, (f) leading flap side edge, (g) strake at low Reynolds number and high angle of attack, (h) wind tunnel, (i) strake tone at high Reynolds number and low angle of attack, (j) outer nacelle, (k) slat edge, (l) flap track, (m) wing tip, and (n) slat resonance. The horizontal grid lines depict $\Delta 20\,$dB. The frequency modification exponents m, the Mach scaling exponents n, and the corresponding angles of attack α and Reynolds numbers are given in Table IV.

- The slats feature Strouhal number scaling peaks with overtones that decay in level and prominence with increasing frequency [see Fig. 7(a)]. They are mainly located at or between the slat tracks, see Fig. 5 source locations 2, 4, 8, 9, 17, 20, 21, and 28.
- The slat tracks scale over Helmholtz number [see Fig. 7(b)]. At high frequencies, they often exhibit a Helmholtz scaling hump that is Mach number dependent. In Fig. 5, they are at the source locations 2, 3, 4, 7, 8, 9, 11, and 16.
- The slat tones feature extremely dominant Strouhal number scaling small-band tones [see Fig. 7(c)]. They are

TABLE IV. Generalized frequency exponents m, Mach scaling exponents n, angles of attack α, and Mach averaged Reynolds numbers $\langle Re \rangle_M$ for the displayed sources in Fig. 7.

	(a)	(b)	(c)	(d)	(e)	(f)	(g)
m	0.90	0.00	0.75	0.00	1.09	0.00	0.71
n	4.44	5.47	3.43	4.23	4.43	4.09	3.43
α [°]	3	5	9	9	3	5	9
$\langle Re \rangle_M$ [1×10^6]	1.4	1.4	1.4	1.4	1.4	10.6	1.4
	h)	i)	j)	k)	l)	m)	n)
m	0.00	0.94	0.00	1.00	0.00	0.66	0.00
n	3.87	3.68	5.47	3.26	6.07	3.59	5.26
α [°]	10	3	5	10	3	9	1
$\langle Re \rangle_M$ [1×10^6]	2.5	10.6	1.4	10.6	1.4	1.8	1.4

mainly located at the slat positions, see Fig. 5 locations 4, 7, 9, 11, 16, 21, 22, 25, and 28.

- The flap (track) tones feature a small Helmholtz scaling tone and are a sub-category of the flap track [see Fig. 7(d)]. In Fig. 5, they are at locations 23, 29, and 32.
- The trailing flap side edges (TFSE), Fig. 5 at location 12, feature a prominent Strouhal scaling peak [see Fig. 7(e)].
- The leading flap side edges (LFSE), Fig. 5 at location 6, feature a smaller Helmholtz scaling peak [see Fig. 7(f)]. At increasing Reynolds numbers, a second Helmholtz number scaling peak emerges.
- The strakes feature a Strouhal number scaling hump [see Fig. 7(g)]. It increases in intensity with increasing angle of attack and disappears with increasing Reynolds number. In Fig. 5, they are at locations 18 and 26.
- The wind tunnel noise, Fig. 5 at location 31, scales over Helmholtz number [see Fig. 7(h)]. It appears next to the wing and is considered as a spurious noise source in this measurement (Ahlefeldt, 2013).
- The strake tone, Fig. 5 at location 18, is a dominant Strouhal scaling tone [see Fig. 7(i)]. It appears only at high Reynolds numbers and low angles of attack and decreases in intensity with increasing angle of attack. It is a sub-category of the strake.
- The outer nacelle area, Fig. 5 source location 13, features a broadband hump that scales over Helmholtz number [see Fig. 7(j)].
- The slat edge is located close to the wing tip, Fig. 5 position 10, and its noise scales over Strouhal number [see Fig. 7(k)]. The spectrum level decays over frequency and

features an additional, low-level Helmholtz scaling hump at high frequencies. It is a sub-category of the slat track.
- The flap tracks feature a low-level Helmholtz number scaling hump [see Fig. 7(l)]. They are located in Fig. 5 at locations 23, 29, and 32.
- The wing tip, Fig. 5 source location 27, features a Strouhal number scaling hump [see Fig. 7(l)], that increases in intensity with increasing angle of attack. The spectra are often contaminated with wind tunnel noise.
- The slat (track) resonances exhibits strong, Helmholtz number scaling peaks and are a sub-category of the slat track, see Fig. 7(n)]. In Fig. 5, they are at the slat tracks 1, and 5.

The fuselage (Fig. 5 location 19), nacelle track (appearing only at very high Reynolds numbers at location 30 in Fig. 5, scaling over Helmholtz number with a very high Mach power exponent $n \approx 7.02$), inner slat gap (Helmholtz scaling hump, similar to the LFSE, location 15 in Fig. 5), and flap gap (location 24 in Fig. 5) are identified and named based on their spatial appearance. Noise occurring at the flap gap was caused by loose tape on the model during the measurement. Additionally, the category slat/slat track is introduced to account for various spectra that are located on the slat or slat tracks but are ambiguous, e.g., the slat/slat track shown in Fig. 3, containing some Strouhal number scaling low-frequency peaks, and some Helmholtz number scaling high frequencies.

The manual source type identification in the A320 dataset is more challenging. The smaller microphone array results in less reliable spectra, especially at low frequencies, and due to the small variation in Mach number the correct scaling behavior and scaling exponent are difficult to identify. Additionally, the typical spectra do not consistently correlate with the spatial appearance of the sources, e.g., the spectra are different for different flap tracks. Finally, the sources are strongly affected by the large range of Reynolds numbers which often result in sources that are transitioning from one mechanism to another (see Fig. 8). Thus, there are multiple sources that we assign the same label, but that feature different spectra (e.g., the fuselage, the slat tracks, and leading flap side edge, see Fig. 7) , and vice versa. However, many of the sources are similar to the one found in the Do728 dataset (e.g., LFSE, TFSE, strake, strake tone, slat, slat resonance, slat tone). In addition to the Do728 source
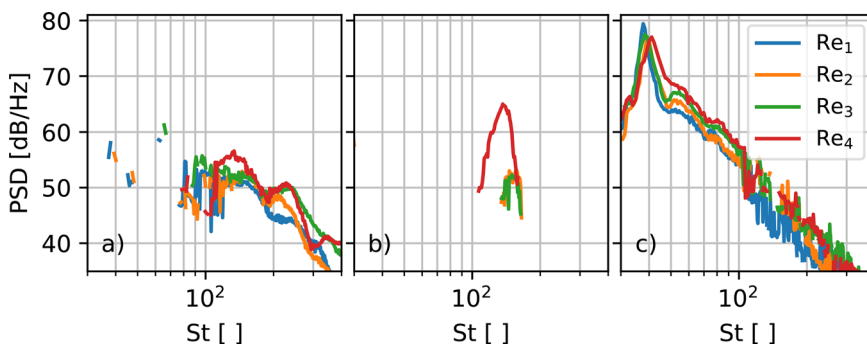

FIG. 8. (Color online) A320. The figure shows the Reynolds number effect on the source types (a) leading flap side edge at $\alpha = 7°$, $M = 0.175$, (b) high Strouhal number scaling tone at $\alpha = 9°$, $M = 0.200$, located on the slat and flap, and (c) trailing flap side edge at $\alpha = 7°$, $M = 0.200$.

J. Acoust. Soc. Am. **151** (2), February 2022

Goudarzi et al.   1269

types, there exist multiple A320 sources on the slat and flap that feature a high Strouhal number scaling tone (high St tone) that increases in intensity with increasing Reynolds number like the strake tone [see Fig. 8(b)].

V. RESULTS

The result section is separated into two parts. First, the results of the aeroacoustic properties and features are presented. Then, based on the resulting feature space, the clustering results are presented.

A. Aeroacoustic feature results

Figure 9 presents the distributions of exemplary features for exemplary source types and compares them between both datasets. The horizontal lines within the distributions display the 0.25, 0.50, and 0.75 percentiles. The exemplary source types were chosen because they were manually identified in Sec. IV with great confidence based on their spectral features in Fig. 7 and they showed interesting acoustical properties. The features were chosen to cover the variety of aeroacoustic properties introduced in Sec. III C.

Figure 9 shows the self-similarity over the modified Strouhal number [FIG. 9(a)] and the Helmholtz number [Fig. 9(b)], see Sec. III C 1. Based on the exemplary source spectra in Fig. 7 and the aeroacoustic literature, we expect the slat track, slat resonance, and leading flap side edge to strongly scale over the Helmholtz number and the slat tone, strake, trailing flap side edge, slat, and strake tone to strongly scale over the (modified) Strouhal number. For the slat tracks, the feature does not achieve satisfying results since it wrongly predicts a strong self-similarity over the Strouhal number for both datasets. The reason for this is the strong decay in SPL over frequency, which dominates the correlation stronger than the local spectral features such as tonal peaks or humps. For the Do728 strake tones, a low Strouhal self-similarity is wrongly predicted. This is due to the inclusion of the p-value in Eq. (9), which becomes large for small-band sources. For the A320 slat tone and LFSE the feature is not robust and results in a large range of values. The expected self-similarity over the Helmholtz number is well captures in Fig. 9(b). This is also true for Strouhal number scaling slat sources with additional Helmholtz scaling high-frequency content, see Fig. 8(a) at $100 \leq St \leq 200$.
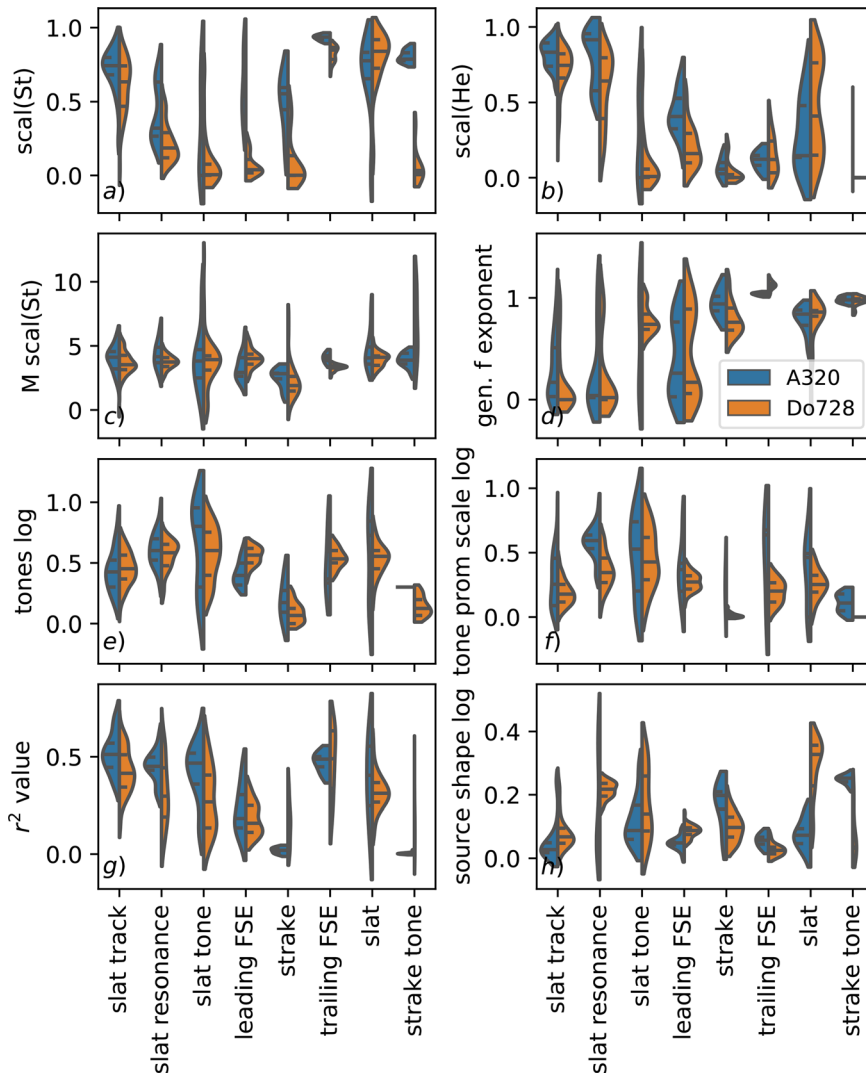

FIG. 9. (Color online) Violin plot comparison of the A320 (blue) Do728 (orange) for exemplary source types and exemplary features from Table III. (a) Shows the broadband self-similarity over the modified Strouhal number, see Sec. III C 1. (b) Shows the broadband self-similarity over the Helmholtz number. (c) Shows the Mach power scaling over the modified Strouhal number, see Sec. III C 3. (d) Shows the generalized frequency modification exponent, see Sec. III C 2. (e) Shows the logarithmic number of tones, and (f) shows the gamma distribution's logarithmic scale of the tone prominence, see Sec. III C 4. (g) Shows the r^2-value of the linear regression of the spectrum, see Sec. III C 7, and (h) shows the logarithmic spatial source shape, see Sec. III C 6.

Figure 9(c) shows the Mach power scaling over the modified Strouhal number. Similar power scalings around M scal(St) ≈ 3.73 (averaged over the displayed source types) are observed. This is expected as aeroacoustic noise is known to scale within a small range (e.g., M^4 for monopoles, M^6 for dipoles, and M^8 for quadrupoles), depending on the source mechanism. However, the variance within the source types often exceeds the variance between the source types. Also, as seen for the trailing flap side edge the Mach scaling can differ for the same source type for different datasets. At this point, it is not clear if this is caused by the assumptions of the method (e.g., ignoring the source directivity) or by the different model geometries.

Figure 9(d) shows the generalized frequency normalization exponent m, see Sec. III C 2. Most of the slat tracks and slat resonances show an exponent around $m \approx 0$. This indicates a Helmholtz scaling and corresponds to the presented self-similarities. For both datasets, there are two groups of LFSE, one that features $m \approx 0$, and one that features $m \approx 1$. For the Do728 strakes, a mean exponent $m \approx 0.79$ is observed, for the A320 strakes $m \approx 0.95$. For the Do728 TFSE $m \approx 1.13$ is observed, for the A320 $m \approx 1.06$. For the Do728 slat $m \approx 0.78$ is observed, for the A320 $m \approx 0.72$.

Figure 9(e) shows the Mach averaged occurrence of tones (logarithmic), see Sec. III C 4. Some source types feature few tones, i.e., the strake and strake tone, some source types feature many tones, i.e.,the slat tones. Figure 9(f) shows the corresponding scale parameter of the tone prominence distribution (logarithmic). A large scale parameter indicates that the distribution is spread out, including tones with small and large prominence. A small scale parameter indicates that all tones have a similar prominence. Both datasets show similar distributions for the features. Generally, the features correspond to our expectations. However, the gamma distribution approximation fails for sources that contain only one prominent tone, such as the Do728 strake tone sources.

Figure 9(g) shows the spectrum shape r^2 based on a linear regression, see Sec. III C 7. For the Do728 the distributions of the strake, the TFSE, and the strake tone are spread out compared to the A320 distribution. Overall, they show similar trends. The feature mainly highlights the fact, that many aeroacoustic sources are broad-band sources with a linear decay in SPL over logarithmic frequency and correctly identifies small-band sources such as the strake and strake tone.

Figure 9(h) shows the source shape (logarithmic). A value close to zero indicates a point source, an increasing value indicates a line source. The results directly depend on the output of SIND, which correctly identified the slat track, LFSE, strake, and TFSE as point-like sources. The Do728 slat was correctly identified as a line-like source. However, the A320 slats were wrongly identified as point-like sources. While SIND yielded overall comprehensible results, on some occasions sources were wrongly spatially separated or combined; e.g., the slat tones sometimes appear on slat track positions and, thus, are identified as point-like sources while

they should be line-like sources (Dobrzynski and Pott-Pollenske, 2001).

Figure 10 shows a Pearson correlation coefficient heatmap for the Do728 feature space. On the top, a feature hierarchy is displayed based on hierarchical clustering with a correlation distance metric based on the Unweighted Pair Group Method with Arithmetic mean (UPGMA) algorithm. This hierarchy shows which features are similar to each other based on the displayed correlations to all other features. The heatmap and hierarchy show that many of the introduced features correlate strongly, especially features that were introduced together to cover an aeroacoustic property such as tonality, or self-similarity. The feature hierarchy shows that these features originate from the same branch. From left to right, the first major branch includes the linear regression's slope (log), the source movement, the generalized frequency exponent, and the source compactness. The first three features correlate negatively with the features that correspond to the tonality and form a sub-branch. The second main branch on the right contains all other features. Its left sub-branch contains the Mach scaling over Strouhal number, and Helmholtz number, as well as the linear regression's
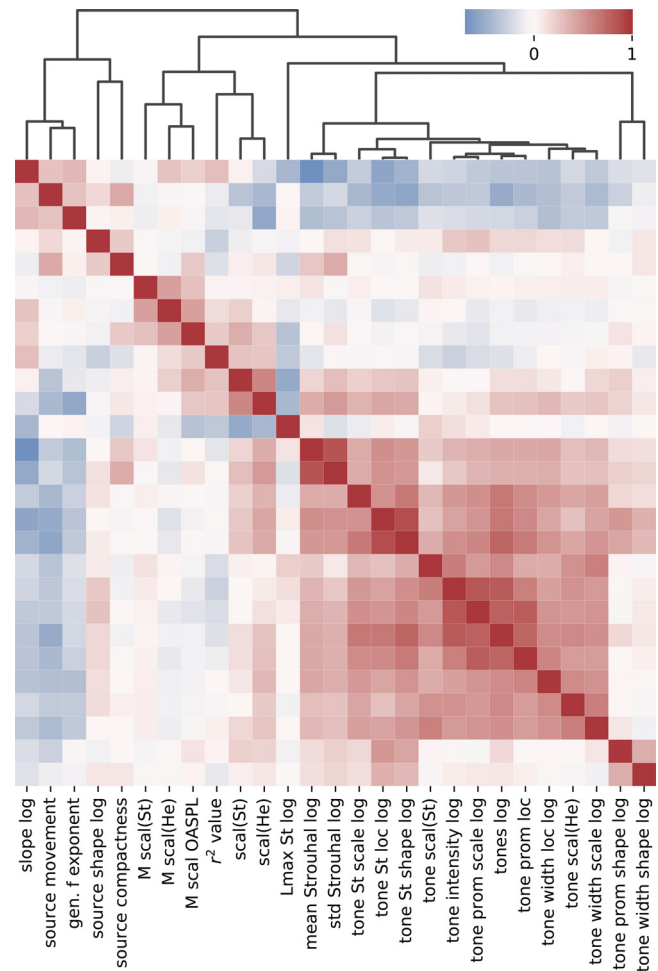

FIG. 10. (Color online) Heatmap of all Do728 feature Pearson correlation coefficients and their hierarchy based on hierarchical clustering with a correlation distance metric (top).

J. Acoust. Soc. Am. **151** (2), February 2022

Goudarzi *et al.* 1271

r^2-value, and the self-similarity (scal) over Strouhal number and Helmholtz number. The other branch contains all features that describe the frequency content of the spectrum [St_{Lmax}, mean, and standard deviation (std) of occurring Strouhal numbers] and its strongly correlated tonality features.

Figure 11 shows a Uniform Manifold Approximation and Projection for Dimension Reduction (McInnes *et al.*, 2018) (UMAP) of the Do728 sources. The colors and symbols both represent the manual labels. UMAP estimates a manifold that locally (and to some extend globally) preserves the data structure in a low dimensional space, based on which the data can be displayed in low-dimensional space. UMAP requires a distance metric, such as a spatial metric (e.g., Mahalanobis, Minkowski), or a similarity metric (e.g., cosine, correlation). All mentioned metrics yield similar results for the presented feature space. Figure 11 shows a 2D space in which we can observe how similar source types are in the introduced feature space and how well the introduced feature space separates the proposed source types. The slat track and slat edge sources are similar, and gradually transition to slat/track sources, and then to slat sources. These groups are not well separated which corresponds to our own assessment since the spectra often smoothly transition from one shape to another and show great variance. The slat tone sources are not captured well in the feature space since they are manually identified with very high confidence, but do not form a well separated group. Other source types such as the wing tip and the trailing flap side edge are well captured in the feature space and show little variance. Overall, the figure shows that sources of the same manually introduced source type are close to each other in the introduced feature space. The ability of
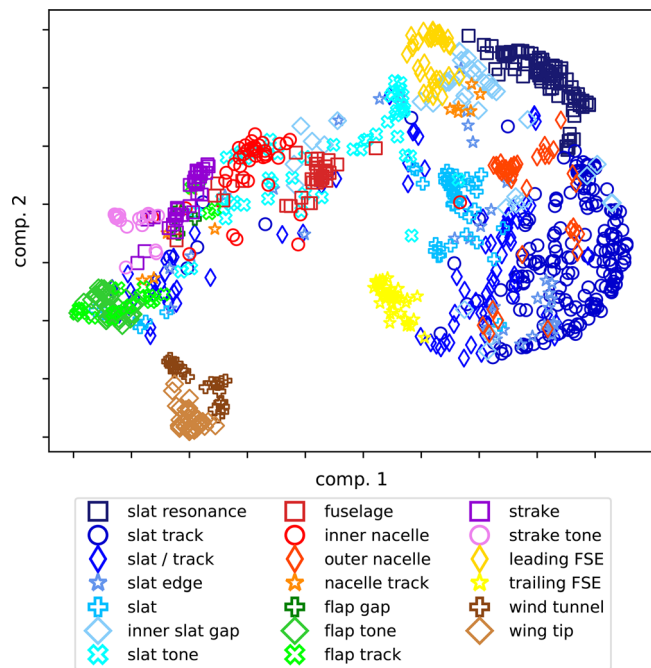
UMAP to form separable source type groups highlights two results. First, the introduced feature space captures sufficient aeroacoustic information for the presented sources, under the condition that the labeling is correct. Thus, groups of multiple sources are formed in the UMAP based on the feature space. Second, the labeling is sufficiently good under the condition that the feature space correctly captures the sources' aeroacoustic behavior. Thus, the groups mainly contain unique source types. Since the source types were identified manually based on the source spectra and not on the introduced feature values, see Sec. IV, this indicates that the label choices are reasonable.

B. Clustering results

The results presented are based on the Do728 and A320 datasets, obtained from sparse beamforming maps with SIND and CRAFT. For the Do720, a minimum sample size of seven was used for HDBSCAN. CRAFT determined fifteen source clusters. Figure 12 shows a confusion matrix of the manually determined labels, see Sec. IV, and the clustering results. The matrix shows how often a source from a manually determined category was clustered into the

FIG. 11. (Color online) Do728. UMAP (McInnes *et al.*, 2018) components for $n_{components} = 2$, $n_{neighbors} = 90$ ($\approx 10\%$ of the dataset), and a correlation distance metric for the presented feature space.

Legend:
- slat resonance
- slat track
- slat / track
- slat edge
- slat
- inner slat gap
- slat tone
- fuselage
- inner nacelle
- outer nacelle
- nacelle track
- flap gap
- flap tone
- flap track
- strake
- strake tone
- leading FSE
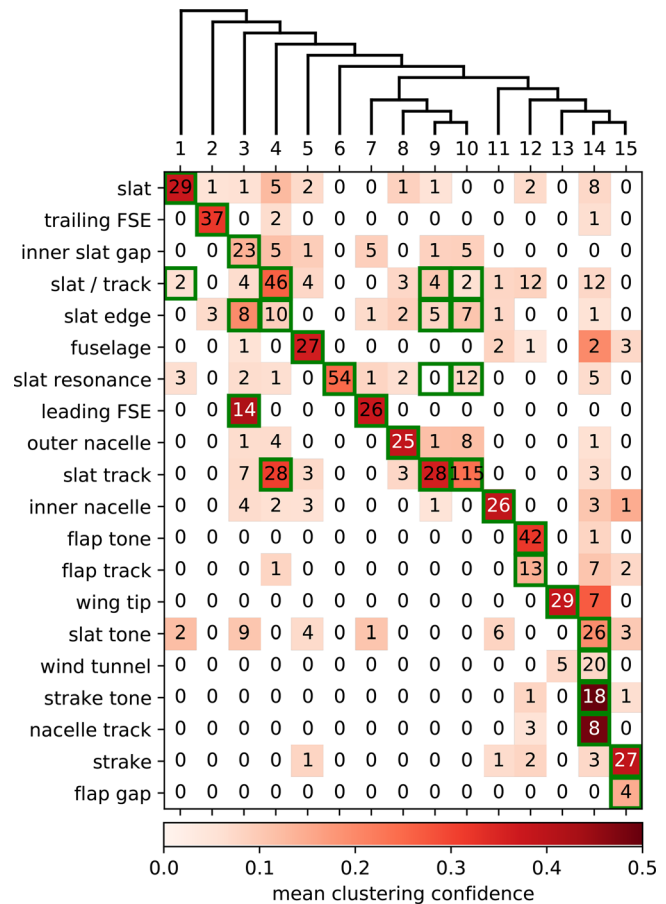- trailing FSE
- wind tunnel
- wing tip

FIG. 12. (Color online) Do728, confusion matrix of the occurrences of our manually identified source types in CRAFT's determined clusters. The color intensity displays the mean clustering confidence. Cluster choices we consider correct are marked with a green box. The tree above the clusters displays their hierarchy.

1272   J. Acoust. Soc. Am. **151** (2), February 2022
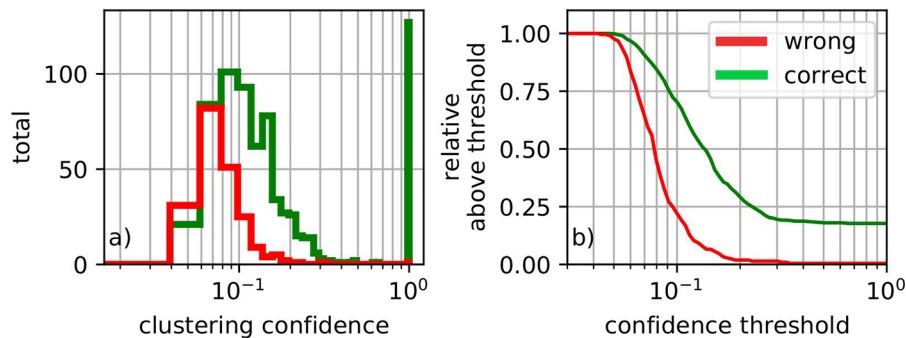
Goudarzi *et al.*

FIG. 13. (Color online) Do728, (a) shows a histogram of the total wrong and correct cluster choices over their clustering confidence. (b) shows the relative number of cluster choices above the confidence threshold t_C on the x axis.

corresponding clusters. Given the manual source type identification is correct, a perfect clustering would result in a cluster group for every manual label and all corresponding sources would be clustered within their corresponding group. Thus, a perfect clustering would achieve a square confusion matrix with all results on the diagonal. The underlying color in the confusion matrix depicts the mean clustering confidence. Since most clusters correlate to the manual labels (they are mostly located on the diagonal axis), our definition of correct clustering results (which are marked with a green box in the confusion matrix) will be based on its comparison to the manual labels.

To identify the clusters which correspond to the manual labels we will take the occurrences of source types per cluster, their estimated confidence, their similarity to other source types, and the cluster hierarchy into account. Thus, cluster number one is assigned to the slat sources. We consider slat sources that are assigned to cluster one as correct clustering results, slat sources assigned to other clusters are considered as wrong clustering results. A slat resonance which was categorized as cluster number nine or ten (which consists mainly of slat tracks) instead of cluster number six (which consists solely of slat resonances) is considered correct since it is a sub-type of a slat track source. All sub-categories that are clustered with their super-categories are considered correct, but not vice versa. Thus, slat tracks that are clustered in group six (slat resonances, a sub-category of slat tracks) are considered wrong. Slats and slat tracks that fall in cluster four (slat/slat track) and vice versa are considered correct, which is a super-category of these ambiguous sources. Cluster numbers 3, 4, 14, and 15 comprise multiple source types. As long as the corresponding source types were assigned to the cluster that contained most of the sources, they are considered correct. The slat tracks occupy the two clusters number nine and ten with high clustering confidence, which we consider as equally correct, as the clusters are both branches of a super-cluster. The leading flap side edge occupies both cluster numbers three and seven with high confidence, thus we consider both clusters as correct. All other clustering results are considered as wrong.

Note that the following clustering assessment is based on both our manual source labeling and our manual definition of correct confusion matrix entries. In total, 213 out of 928 Do728 source predictions (22.95%) are considered wrong and 715 (77.04%) are considered correct. Figure 13(a) shows

the number of clustering choices at the given clustering confidence. Both the correct and wrong clustering choices decrease with increasing confidence. Figure 13(b) shows the relative number of wrong and correct clustering choices that lie above the confidence threshold t_C. We observe that the wrong clustering results decrease much more rapidly than the correct clustering results. As an example, if the clustering results with confidence below $t_C = 0.1$ are discarded, only a prediction for 59.26% of the sources is retained, but the clustering accuracy increases to 91.45%.

Figure 14 shows the confusion matrix of our manually identified source types and the clustering results for the
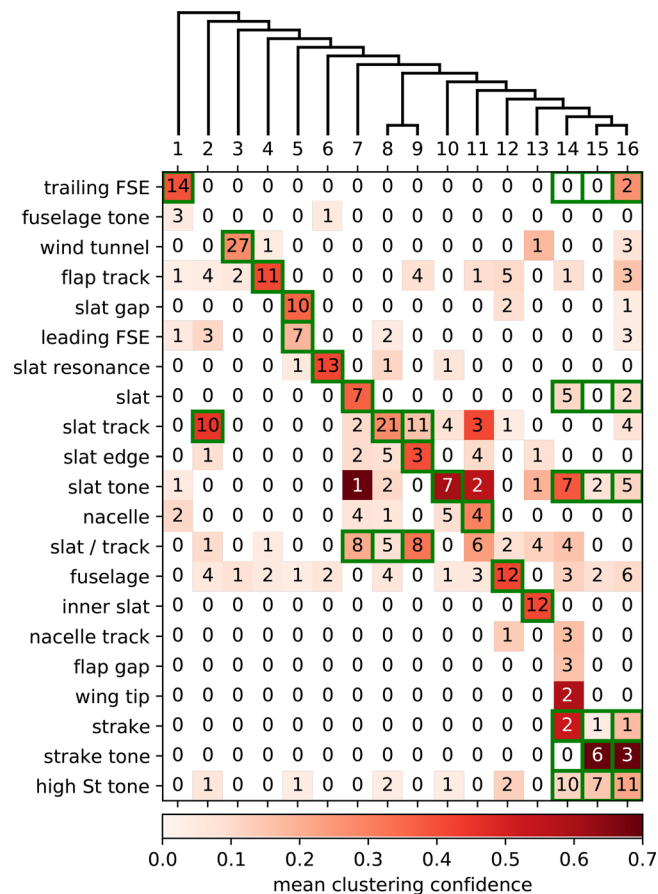

FIG. 14. (Color online) A320, confusion matrix of the occurrences of our manually identified source types in CRAFT's determined clusters. The color intensity displays the mean clustering confidence. Cluster choices we consider correct are marked with a green box. The tree above the clusters displays their hierarchy.

J. Acoust. Soc. Am. **151** (2), February 2022

Goudarzi *et al.*   1273

A320. The correct clusters are determined as stated above for the Do728. In particular, the super-cluster 14, 15, and 16 represent Strouhal number scaling tones. Thus, we consider the clustering results for the nacelle track, flap gap, and wing tip as wrong. The super-clusters 7, 8, and 9 represent slat/tracks, with sub-cluster 7 including the slats, and sub-clusters 8 and 9 including the slat tracks and the slat edge. In total, 154 out of 408 source predictions (37.75%) are wrong and 254 (62.25%) are correct. As shown for the Do728 results, if the clustering choices with confidence below $t_C = 0.1$ are discarded, only a prediction for 51.47% of the sources is retained, but the clustering accuracy increases to 74.29%.

VI. DISCUSSION

CRAFT is built on the assumption that an aeroacoustic source is driven by a mechanism that reveals its nature over the variation of the Mach number. The limitation of this general assumption is that we neglect any changes of the source mechanism over the Mach number. We showed in Fig. 3(b) at high Helmholtz numbers that sources can exhibit a substantial Mach dependency, which is not captured by the proposed method.

Based on this assumption, we proposed a variety of features in Sec. III C that are supposed to formalize aeroacoustic properties and that are robust towards degraded spectra. This is necessary to automatically extract the source spectra, their positions, and their spatial distribution. The resulting source spectra are often not very reliable at low frequencies or contain missing values. This is especially problematic since their dominant SPL, which is preferred in many features, occurs at these low frequencies. We neither claim that the list of the properties is complete and covers all acoustic phenomena nor do we claim that the feature calculation is robust in all data scenarios. We hope to spark a discussion in the acoustic community on which properties are important for which source types, how these can be broken down to numeric feature values, and how they can be calculated robustly and efficiently.

In Sec. III C 1, we presented a calculation method to determine how self-similar the source spectra are over a given frequency type, i.e., the Helmholtz and Strouhal number. For several source types, the feature does not achieve satisfying results. The reason for this is the strong decay in SPL over frequency, which dominates the correlation stronger than the local spectral features such as tonal peaks or humps. We encourage the community to propose a mathematical definition that fixes these issues.

In Sec. III C 2, we showed that the normal Strouhal number definition is not sufficient when working with source spectra at different Reynolds numbers. Thus, we defined a normalized frequency that is a generalization of the Strouhal and Helmholtz number. that some source mechanisms increase their frequency dependency on the Mach number, while others decrease their Mach dependency. At these conditions, the increase in Reynolds number with increasing Mach number is much stronger than at ambient conditions, which should result in a stronger drift of the frequency and thus, a correlation. To our knowledge, this is the first time this phenomenon is described, but it is too complex to be fully covered within the scope of this paper. More research is necessary to understand the underlying acoustic mechanisms and the implications on wind tunnel measurements.

In Sec. III C 3, we introduced a method to determine the power exponent for a separate scaling over the Strouhal and Helmholtz number using a weighted standard deviation between the spectra, see Eq. (15). However, since we assumed only small changes in the Mach number, and based on the small amount of observed Mach numbers, the correct determination of the power exponent is difficult which causes large variances within source types, which are larger than the variances between different source types.

In Sec. III C 4, we introduced a variety of features to describe the tonality of the spectra. Figure 10 shows that the tonality features are highly correlated and belong to the same branch of the feature hierarchy. At this point, it is not clear if the tonal behavior can be captured by fewer features with less correlation.

In Sec. III C 5, we introduced a method to detect if sources move with increasing Mach number, and in Sec. III C 6, a method to detect if the source is point-like or line-like. These features can only be used in combination with beamforming or other acoustic imaging methods. The results suggest that the source movement feature currently estimates the position uncertainty instead of the true movement of sources (e.g., downstream moving vortex detachments). Figure 10 showed that the source movement, the source shape, and the source compactness are mostly correlated and that they belong to the same branch in the feature hierarchy. This suggests that they are subjected to an underlying, yet unknown, phenomenon.

In Sec. III C 7, we introduced features to determine the general shape of the spectra and their frequency content. Figure 10 showed that the r^2-value is closely related to the self-similarity and scaling behavior, the slope is rather connected to the spatial source shape, and the frequency content (mean and std Strouhal number) is connected to the tonality. This suggests that the current definition of the spectrum shape does contain source type-dependent variance, but does not capture a basic aeroacoustic property.

To evaluate the quality of the features and CRAFT, we labeled the presented datasets manually. We showed in Fig. 11 that sources can gradually shift their spectrum shape with increasing Reynolds number and that they can feature multiple frequency regions with different mechanisms (see Fig. 8). Thus, we heavily relied on meta-information for the manual source type identification such as the source position. Since the proposed method was designed to overcome exactly this problem, the resulting metrics should be evaluated with caution. Also, the labeling was not performed by independent researchers.

To assess the combined quality of the feature space and of the manual labels we performed the dimensionality reduction and manifold estimation (UMAP) in Fig. 11 to visualize the data in two dimensions. The distance between the source groups, their distribution density, and their connections relate well to our observations in Sec. IV. Also, the source type distribution emphasizes the problem of manually labeling the sources based on their spectra, because source types gradually transition from one to another category, e.g.,the slats that gradually transition to slat track noise. Figure 8 also showed that a single source location can gradually or abruptly change its mechanism with increasing Reynolds number. However, Fig. 11 showed that the source groups are reasonable with respect to their members distribution in the introduced feature space.

We used HDBSCAN (Campello *et al.*, 2013; McInnes *et al.*, 2017) to cluster the sources without any prior assumption of the expected number of source types or source distributions in the feature space. For the Do728, the resulting clusters related well to our manual evaluation (see Fig. 12). This is a promising result since the feature space not only captures enough information to separate most of the source types, but the variance between the different source types is also greater than the variance of an unwanted phenomenon. Since our source identification was often ambiguous and since not all clusters related to our labels the exact accuracy of CRAFT and the reason for the wrong cluster choices is up for debate. Our evaluation of the Do728 clustering was based on the confusion matrix in Fig. 12 and resulted in an accuracy of 77.04%.

The usefulness of the chosen clusters can only be evaluated qualitatively based on their consistency, their ability to separate source mechanisms from each other, and detecting sources for which the spatial location is misleading. For airframe noise, typical analyzed source regions are the whole slat, flap, flap side edge, and nacelle region, including the strakes (Ahlefeldt, 2013, 2017). Regarding the Do728 slat region, CRAFT showed that typical slat sources are distinctly different from slat track sources based on the cluster hierarchy. Occasionally, slat tones appeared with decreasing probability towards high Reynolds numbers. Often, they occurred at the slat positions but at different angles of attack (slat noise appeared mainly at low angles of attack). CRAFT was able to separate these phenomena very well. However, multiple source types were clustered into the single cluster 14. Decreasing the sample size for HDBSCAN eventually results in a separation of these sources but also numerous sub-clusters for the other source types.

For the A320, CRAFT's clusters did loosely correlate to our manually identified source types and thus, the accuracy of the result was much more difficult to evaluate. We encourage the readers to interpret the confusion matrix results based on their own experience. The evaluation based on our confusion matrix assessment in Fig. 14 resulted in an accuracy of 61.52%. The lower clustering accuracy can be accounted to the larger feature variance compared to the Do728 sources, as depicted in Fig. 9. This is mainly caused by the worse quality of the spectra, due to the smaller microphone array employed for the measurements.

VII. CONCLUSION

The goal of this paper was to use clustering to group multiple sources based on their aeroacoustic properties to reveal underlying physical mechanisms and guide the acoustic expert in identifying and analyzing the sources correctly. The general assumption of this EDSS "CRAFT" was that the physical mechanism of a source can be determined by the change of its properties over the Mach number. Thus, source measurements at multiple flow speeds are required. Example data of Dornier 728 and Airbus A320 CLEAN-SC beamforming maps were used at different flow speeds, angles of attack, and Reynolds numbers to derive the aeroacoustic properties and employ the presented method.

To reduce the complex acoustic properties to a data space that can also be understood by the machine, we introduced a feature-set that expresses these properties as a combination of single, numerical values. These features are independent or averaged over the spectra at different Mach numbers, which enables CRAFT to compare and cluster sources from different experiments. To further evaluate the data, we presented exemplary source spectra and corresponding manual labeling of the sources. We showed that the manual labeling of the sources is often ambiguous due to degenerated spectra, multiple source mechanisms, or Reynolds number dependent trends, which resulted in additional uncertainty. Despite the ambiguous manual source type identification, many source types formed distinguishable distributions in the introduced feature space, which was visualized with a Uniform Manifold Approximation and Projection for Dimension Reduction.

We used Hierarchical Density Based Clustering for Applications with Noise to group the sources in the introduced feature space, which did not include meta-information such as the source position, the angle of attack, or the Reynolds number. The clusters corresponding mostly to the manually identified source types were consistent between the datasets and provided the necessary information to identify sources that behaved atypically for their spatial locations. For example, it allowed the correct identification of multiple source types that were all located on a single slat position. The result also provided a confidence estimation for the clustering results. We showed that sources are mostly clustered wrongly by CRAFT at low confidence, while the clustering with high confidence is mostly correct. Experts can discard predictions below a confidence threshold, which further increases the prediction accuracy.

For future work, we plan to analyze more data with the introduced method to further evaluate the quality and reliability of the proposed features. We also hope to start a discussion in the aeroacoustic community on the selected properties and their corresponding features, possible shortcomings, alternative definitions or calculation methods, and the manual identification of aeroacoustic source phenomena.

ACKNOWLEDGMENTS

Abramowitz, M. (**1974**). *Handbook of Mathematical Functions, with Formulas, Graphs, and Mathematical Tables* (Dover Publications, Inc., Englewood Cliffs, NJ).

Aggarwal, C. C., Hinneburg, A., and Keim, D. A. (**2001**). "On the surprising behavior of distance metrics in high dimensional space," in *Database Theory — ICDT 2001*, edited by J. Van den Bussche and V. Vianu (Springer, Berlin Heidelberg), pp. 420–434.

Ahlefeldt, T. (**2013**). "Aeroacoustic measurements of a scaled half-model at high Reynolds numbers," AIAA J. **51**(12), 2783–2791.

Ahlefeldt, T. (**2017**). "Microphone array measurement in european transonic wind tunnel at flight Reynolds numbers," AIAA J. **55**(1), 36–48.

Ben Ali, J., Saidi, L., Harrath, S., Bechhoefer, E., and Benbouzid, M. (**2018**). "Online automatic diagnosis of wind turbine bearings progressive degradations under real experimental conditions based on unsupervised machine learning," Appl. Acoust. **132**, 167–181.

Bianco, M. J., Gerstoft, P., Traer, J., Ozanich, E., Roch, M. A., Gannot, S., and Deledalle, C. A. (**2019**). "Machine learning in acoustics: Theory and applications," J. Acoust. Soc. Am. **146**(5), 3590–3628.

Campello, R. J. G. B., Moulavi, D., and Sander, J. (**2013**). "Density-based clustering based on hierarchical density estimates," in *Advances in Knowledge Discovery and Data Mining*, edited by J. Pei, V. S. Tseng, L. Cao, H. Motoda, and G. Xu (Springer, Berlin-Heidelberg), pp. 160–172.

Dobrzynski, W., and Pott-Pollenske, M. (**2001**). "Slat noise source studies for farfield noise prediction," in *Proceedings of the 7th AIAA/CEAS Aeroacoustics Conference and Exhibit*, May 28–30, Maastricht, the Netherlands.

Goudarzi, A., Spehr, C., and Herbold, S. (**2020**). "Expert decision support system for aeroacoustic classification from deconvolved beamforming maps," in *Proceedings of AIAA Aviation 2020*, June 15–19, Virtual.

Goudarzi, A., Spehr, C., and Herbold, S. (**2021**). "Automatic source localization and spectra generation from sparse beamforming maps," J. Acoust. Soc. Am. **150**, 1866–1882.

Howe, M. S. (**2007**). *Hydrodynamics and Sound* (Cambridge University Press, Cambridge, UK).

Karabasov, S. A. (**2010**). "Understanding jet noise," Philoso. Trans. R. Soc. A **368**(1924), 3593–3608.

Lighthill, M. J., and Newman, M. H. A. (**1952**). "On sound generated aerodynamically I. General theory," Proc. R. Soc. London. Ser. A **211**(1107), 564–587.

McInnes, L., Healy, J., and Astels, S. (**2017**). "hdbscan: Hierarchical density based clustering," J. Open Source Softw. **2**(11), 205.

McInnes, L., Healy, J., and Melville, J. (**2018**). "UMAP: Uniform manifold approximation and projection for dimension reduction," J. Open Source Softw. **3**(29), 861.

Mello, R. F., and Ponti, M. A. (**2018**). *Machine Learning* (Springer International Publishing, New York).

Merino-Martinez, R., Sijtsma, P., Rubio Carpio, A., Zamponi, R., Luesutthiviboon, S., Malgoezar, A., Snellen, M., Schram, C., and Simons, D. (**2019**). "Integration methods for distributed sound sources," Int. J. Aeroacoust. **18**, 444–469.

Merino-Martínez, R., Sijtsma, P., Snellen, M., Ahlefeldt, T., Antoni, J., Bahr, C. J., Blacodon, D., Ernst, D., Finez, A., Funke, S., Geyer, T. F., Haxter, S., Herold, G., Huang, X., Humphreys, W. M., Leclère, Q., Malgoezar, A., Michel, U., Padois, T., Pereira, A., Picard, C., Sarradj, E., Siller, H., Simons, D. G., and Spehr, C. (**2019**). "A review of acoustic imaging methods using phased microphone arrays," CEAS Aeronaut. J. **10**(1), 197–230.

Michalke, A. (**1977**). "On the effect of spatial source coherence on the radiation of jet noise," J. Sound Vib. **55**(3), 377–394.

Müller, E.-A. (**1979**). *IUTAM Symposia Mechanics of Sound Generation in Flows* (Springer-Verlag, Berlin Heidelberg).

Ozanich, E., Thode, A., Gerstoft, P., Freeman, L. A., and Freeman, S. (**2021**). "Deep embedded clustering of coral reef bioacoustics," J. Acoust. Soc. Am. **149**(4), 2587–2601.

Prandtl, L., and Tietjens, O. (**1957**). *Applied Hydro and Aeromechanics* (Dover, Englewood Cliffs, NJ).

Quinlan, D., and Krane, M. (**1996**). "Aeroacoustic source identification using frequency dependent velocity scaling," in *2nd AIAA/CEAS Aeroacoustics Conference*, May 6–8, State College, PA.

Schölkopf, B., Smola, A., and Müller, K.-R. (**1998**). "Nonlinear component analysis as a kernel eigenvalue problem," Neural Comput. **10**(5), 1299–1319.

Sijtsma, P. (**2007**). "Clean based on spatial source," Int. J. Aeroacoust. **6**, 357–374.

Thorndike, R. L. (**1953**). "Who belongs in the family?," Psychometrika **18**, 267–276.

Zdravkovich, M. M. (**1997**). *Flow Around Circular Cylinders* (Oxford University Press, Oxford, UK), Vol. 1.

1276   J. Acoust. Soc. Am. **151** (2), February 2022

Goudarzi *et al.*